ADVANCED FUNCTIONAL MATERIALS
www.afm-journal.de

Sonication-Assisted Palladium Nanogaps in a Capacitive Structure: A Tunable and Reliable Solution for Sensitive Hydrogen Monitoring

Sang-kil Lee, Joonho Lee, Jiwoo Hong, Seyoung Park, Eugene Cho, Seunghyun Lee, Keunhyung Lee, Hyun-Sook Lee, Kyu Hyoung Lee, and Wooyoung Lee**

Pd nanogap hydrogen sensors rapidly and selectively detect H_2 through hydrogenation-induced volumetric expansion of the Pd lattice. However, this type of resistive sensor faces challenges in ensuring reliability due to the difficulty of precisely controlling nanogaps formed within the potential conduction paths. Herein, a novel H_2 sensor is proposed that utilizes a capacitive mechanism to substantially improve both sensitivity and reliability. Simple ultrasonication is employed to create Pd seed cracks, which evolve into uniform nanogap networks following initial phase transitions (α-PdH $\rightarrow$ β-PdH). In the Pd/PDMS/Doped-Si system, capacitive response driven by the area change of the upper electrode accurately reflects real-time nanogap behavior in response to H_2, producing stable signals within a defined range of values. The initial crack density, adjustable by varying the sonication time, allows for customizable gap sizes and detection ranges, achieving sub-20 nm gaps and an ultra-low detection limit of 3 ppm. Repeatability tests using 300 ppm H_2 over 50 cycles demonstrate exceptional durability and signal stability at low concentrations, surpassing previous Pd nanogap sensors. This capacitive sensor provides a reliable and adaptable solution for H_2 detection, marking a significant advancement toward commercializing Pd nanogap sensors.

1. Introduction

Hydrogen (H_2) has long been recognized as an environmentally friendly and efficient energy source. However, its low ignition point, high flammability, and wide explosive range, combined with its colorless and odorless nature, make the immediate detection of leaks challenging.[1,2] Therefore, rapid and accurate H_2 detection is crucial for its safe use. In line with global carbon neutrality efforts, various applications of H_2, such as vehicle fuel cells and H_2 storage systems, have advanced significantly in recent years.[3] Additionally, H_2 generation at the anodes of secondary batteries in electric vehicles and energy storage systems during the initial stages of thermal runaway has been reported.[4,5] Developing H_2 monitoring technology with low limits of detection (LODs), fast and accurate response times, high selectivity, and high reliability is essential for real-time accident prevention and immediate response across various modern industries.

Over the past few decades, various H_2 sensing technologies have been studied. Plasmonic-based optical sensors have gained attention for their high sensitivity and fast response at low temperatures,[6,7] but the complexity and cost of fabrication remain as practical concerns. Chemiresistive sensors offer a simple design with high sensitivity,[8] yet they typically require high operating temperatures and suffer from poor selectivity and environmental instability. Electro-mechanical capacitive sensors have also been explored for their low-power operation,[9–11] but achieving both structural simplicity and high sensitivity has remained a challenge. In this study, we present a room-temperature capacitive H_2 sensor that offers high sensitivity and reliability, while being based on an extremely simple structure and fabrication using sonication-induced palladium (Pd) cracks.

In H_2 sensing, Pd is widely used as a sensing or catalytic material due to its ability to dissociate H_2 molecules and selectively absorb atomic hydrogen even at room temperature.[12] However, because its electrical change during hydrogenation is limited, some resistive sensor studies have alternatively leveraged its mechanical behavior and gap structures to enhance sensitivity.[13–16] Notably, Pd thin-film-based nanogap H_2 sensors can be easily fabricated on elastomeric substrates, offering high sensitivity and rapid response times even at room temperature.[17–26] These sensors act as resistive on/off switches, with distinct conductance changes driven by nanogap motion induced by reversible volumetric change of the Pd lattice in response to H_2

S.-k. Lee, J. Lee, J. Hong, S. Park, E. Cho, S. Lee, K. Lee, H.-S. Lee, K. H. Lee, W. Lee
Department of Materials Science and Engineering
Yonsei University
50 Yonsei-ro, Seodaemun-gu, Seoul 03722, South Korea
E-mail: khlee2018@yonsei.ac.kr; wooyoung@yonsei.ac.kr

The ORCID identification number(s) for the author(s) of this article can be found under https://doi.org/10.1002/adfm.202506017

DOI: 10.1002/adfm.202506017

Table 1. Comparison of the fabrication methods, measurement mechanism, nanogap size, and H_2 (N_2 balance) detection limits of Pd nanogap sensors.

Year	Nanogap formation method		Substrate	Measurement Mechanism	Gap Size [nm]	LOD [ppm]	Refs.
2012	CPE (4% H_2 to uncracked Pd)		PDMS	Resistive	900	4,000	[17]
2013	LNF-induced cracked Pd				87	300	[18]
2011	MOTIFE (Stretching)	Pd			300	4,000	[19]
2012		PdNi			62	100	[20]
2013	LNF-processed Pd				25	200	[18]
2013	Initial H_2 eng. Pd (One-time use)				8	10	[21]
2014	Pd-PMMA hybrid				420	600	[22]
2021	75%-strained Pd (Thermal stability test)				52	300	[23]
2016	Bending	AuPd	PI/Steel foil		30	100	[24]
2020		PdCr			8	10	[25]
2019	Stampped NRB arrays	Nanoimprinted Pd	PUA		60	14,000	[26]
2024	SANG (Sonication-assisted Pd Nanogap)		PDMS/Si	Capacitive	Sub-20	3	This work

concentration. Therefore, achieving uniform and narrow nanogaps in a reproducible manner is critical for realizing sensitive and reliable sensing. While various methods have been proposed for nanogap formation, including exposure to high concentrations of H_2,[17] liquid-nitrogen freezing,[18] and repeated mechanical stretching,[18–23] no technique has yet been shown to simultaneously achieve uniformity, reproducibility, and ease of fabrication. **Table 1** summarizes the reported nanogap formation techniques, gap sizes, and limits of detection (LODs) for Pd nanogap H_2 sensors to date.

In addition, these resistive on/off sensors have two fundamental limitations. First, the LODs and response time are predominantly determined by the widest gap in the conduction path, despite the presence of narrower gaps in the film. This is because the on/off sensors generate signals only when all gaps in a potential conductive path are closed due to sufficient hydrogenation-induced volume expansion, thus exhibiting serial switching circuit characteristics. This makes it difficult for resistive sensors to achieve a low LODs and reduces reliability, as the wide gaps, which are difficult to close at low concentrations, primarily dictate the sensing characteristics. Second, most studies have used unsupported polymer substrates despite the susceptibility of Pd thin films to unintended mechanical strain. Curvature changes during substrate handling directly affect gap characteristics, thereby undermining the reliability of these sensors.

To address various issues in existing H_2 sensing technologies, we developed a new nanogap formation method and H_2 sensor based on a Pd/PDMS/doped-Si capacitive structure. A polydimethylsiloxane (PDMS) layer (≈17 µm thick) was spin-coated onto a doped-Si wafer, and a Pd film (10 nm-thick) was deposited by sputtering. This study presents two key innovations. First, we found that simple ultrasonication can create highly uniform seed cracks in the Pd film. When first exposed to high-concentration H_2, these seed cracks developed into an operational nanogap network with gaps narrower than 20 nm. In Section 2, we confirmed their uniformity, performance reproducibility, and tunability. Second, as a method to monitor the behavior of nanogap networks, we introduced a capacitive sensing mechanism into Pd nanogap sensors for the first time. As H_2 concentration increases, nanogaps close and the effective area of the upper electrode increases, leading to a rise in capacitance. Since this method does not require the formation of a complete conducting path in the Pd film, it is advantageous for high sensitivity. The maximum and minimum signal values are determined by physical parameters rather than the intrinsic properties of the materials, significantly enhancing the reliability of the sensor. Furthermore, the doped-Si substrate serves both as the bottom electrode and as mechanical support, preventing unintentional deformation of the nanogaps and enhancing sensor stability and reliability.

This approach enabled an ultra-low LOD of 3 ppm (N_2 balance), with perfect repeatability over 50 cycles even at low H_2 concentrations (300 ppm). We also found that the density of sonication-induced seed cracks, which can be easily controlled by sonication time, critically determines the average nanogap size. This allowed us to create a highly reliable nanogap sensor with a tunable sensing range. Our sonication-assisted method provides a controllable way to form nanogaps, establishing a solid foundation for developing highly reliable and customizable nanogap-based H_2 sensors. Furthermore, integrating these nanogaps with a capacitive sensing mechanism significantly improves the potential for commercialization and contributes to safer hydrogen energy and advanced secondary battery technologies.

2. Results and Discussion

2.1. The Capacitive Pd Nanogap Sensor with Sonication-Assisted Nanogaps (SANG)

Figure 1a illustrates the structure of the proposed capacitive nanogap sensor, alongside the procedure for obtaining operational nanogaps through sonication-induced Pd cracks. The top-view optical image of our sensor can be found in Figure S1 (Supporting Information). The doped-Si layer in our sensor serves

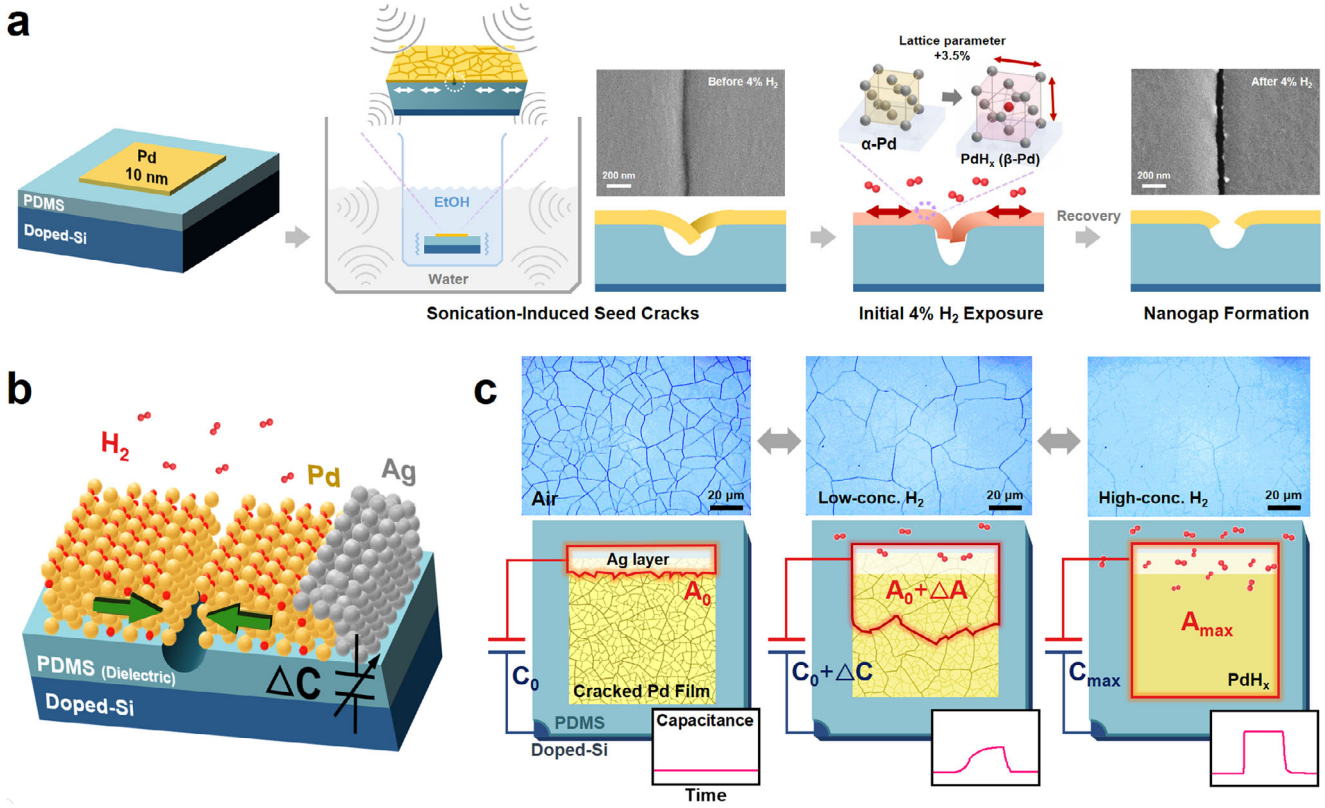

Figure 1. a) Schematic structure and Pd nanogap formation process for the capacitive nanogap sensor. b) Schematic representation of the operational principle of the Pd nanogap sensor. A 10 nm-thick Pd layer was deposited on PDMS as the H_2-sensing component, while a 50 nm-thick Ag layer was partially overlapped with the Pd layer on PDMS to define the base-level signal of the sensor. c) Schematics depicting the mechanism of capacitance changes in the sensor relative to H_2 concentration, accompanied by in situ OM images. When there is no H_2, the Ag layer (white) is electrically isolated from the Pd thin film (yellow) by the Pd nanogaps, resulting in the measurement of the base-level capacitance (C_0) (left image). As the H_2 concentration increases, the area electrically connected with the Ag electrode (red-enclosed) increases owing to contact of the fine Pd gaps (middle image). At higher H_2 concentrations, nanogaps throughout the film are fully in contact (right image).

as the bottom electrode of the capacitor while also providing structural support and mechanical stability of the system. To address the mechanical vulnerability associated with unsupported millimeter-thick PDMS substrates used in previous studies, we applied a thin PDMS film onto a rigid Si wafer via spin-coating. This approach mitigates structural deformation from mechanical stress during handling, thereby enhancing the long-term stability and reliability of the sensors by preventing curvature-induced changes in gap sizes. The peel-off test (Figure S2, Supporting Information) also verifies the stability of the bonding interfaces between Pd and PDMS, as well as between PDMS and SiO_2. Given the use of a stable PDMS substrate supported by a rigid Si layer, traditional mechanical stretching–a common method for forming Pd nanogaps in H_2 sensors[18–23]) was not applicable. Instead, we discovered that ultrasonication serves as an effective alternative for nanogap formation, facilitating precise control over crack density and uniform crack morphology. Based on extensive research on nanogap formation,[17–26] we identified t_{Pd} of 10 nm as optimal. If the Pd films are thinner than this threshold, high substrate-induced constraint can result in continued accumulation of mechanical deformation at the Pd/PDMS interface during prolonged operation,[27] even after gap formation (See Note S1, Supporting Information). Lee et al.[17] reported that in CPE (cracked Pd films on elastomeric substrates) sensors, Pd thin films thinner than 8 nm struggled to close gaps after multiple hydrogenation cycles, leading to a degradation in sensor response. On the other hand, Pd films thicker than 15 nm had difficulty forming effective nanogaps, as the sonication-induced seed cracks failed to remain electrically isolated after the initial H_2 exposure. Therefore, a 10 nm Pd thickness was determined to be ideal for ensuring the formation of operational nanogaps and maintaining reliable sensor performance during low-concentration H_2 cycles. Under these selected structural conditions, we visually confirmed that sonication (5–180 s) in liquid ethanol produced complex networks of fine cracks on the surface 10 nm-thick Pd thin film (Figure S3, Supporting Information). As sonication time increased, stress concentrated on these initial cracks, causing them to propagate and connect, resulting in denser networks. The omnidirectional cavitation from sonication contributed to the uniformity of the crack morphology, a phenomenon that will be quantitatively analyzed in the following section. Although there have been no previous reports of crack induction through sonication in thin-metal-film/soft substrate systems, it is evident that shock waves generated by ethanol cavitation can produce periodic compressive and tensile stresses across the surface.[28–30] The high frequency of these shock waves

limits the system's ability to distribute stress through deformation, leading to significant localized stress accumulation on the brittle metal surface. Cracks readily formed on the Pd surface as the PDMS substrate transitioned from soft to brittle, acquiring silica-like properties during metal deposition.[31,32] The mismatch in mechanical properties between the metal films and the soft polymers, such as PDMS, frequently leads to failures, including wrinkling under compressive stress and cracking under tensile stress, as the stiffer metal film cannot accommodate strain as effectively as the softer substrate.[15,33–35] Moreover, the residual compressive stress induced by sputtering in the Pd thin film[33,34] caused the Pd layers to overlap after crack formation, indicating that not all visually observed cracks resulted in electrically isolated Pd islands. Upon exposing the Pd/PDMS/Si sample to high concentrations of H_2 (4%, balanced with N_2) after sonication, the Pd lattice underwent a phase transition to the β-phase due to hydrogen absorption, leading to a volumetric expansion with a lattice parameter increase of ≈3.5%.[36] During this process, the broken Pd films exerted strong repulsive forces on both ends.[21] Additionally, during the lattice expansion, the PDMS substrate imposed constraint stress on the Pd lattice, which released excess compressive stress above its yield strength through plastic deformation.[27] After several minutes in an H_2 atmosphere, purging with N_2 induced dehydrogenation in the Pd lattice, causing rapid contraction as it reverted to the α-phase. This contraction subjected the plastically deformed Pd film to in-plane tensile stress from the PDMS substrate,[37,38] leading to the electrical separation of the overlapping Pd layers. This mechanism explains the formation of operational Pd nanogaps capable of fast on/off switching in response to H_2 concentration changes, originating from sonication-induced seed cracks. Previous studies have also leveraged hydrogenation-driven phase transitions in Pd thin films to convert initial cracks into operational nanogaps, although different methods were used to induce seed cracks with varying morphologies.[18–26] During the initial stage of high-concentration H_2 exposure and the subsequent stage where the system operates as a H_2 sensor, the thermodynamic conversion of Pd hydride back to Pd upon H_2 removal can be understood from pressure-composition isotherm (PCI) data of Pd under ambient temperature and pressure conditions.[39–43] Additionally,[27] conducted in situ analyses for similar structures (Pd/PDMS/Si) used in this study, which demonstrated reversible changes in lattice parameters during H_2 absorption–desorption cycles at room temperature. The experimental validation of the effects of sonication and subsequent H_2 adsorption/desorption on nanogap formation is discussed in detail in Section 2.2.

Figure 1b illustrates the operational principle of SANG sensors. Unlike traditional resistive nanogap sensors, which measure changes in electrical resistance, our sensor utilizes a capacitive approach to capture the behavior of dense nanogap networks with high sensitivity. The capacitance (C) of the parallel-layered system—comprising a Pd thin film, PDMS (dielectric layer), and a B-doped Si substrate[27] reflects the discrete changes in the area of the Pd electrode caused by the behavior of numerous nanogaps. The C can be described by the following equation:

$$C = \epsilon_r \epsilon_0 \frac{A}{t_{dielectric}} \quad (1)$$

where ϵ_r is the relative permittivity of the PDMS layer, ϵ_0 is the vacuum permittivity, A is the area of the upper electrode in contact with the Ag layer, and $t_{dielectric}$ is the thickness of the dielectric layer. The Pd layer, which could potentially contribute to the upper electrode area, is not conductive across its entire surface due to the presence of numerous nanogaps in its initial state. Therefore, we sputtered a 50 nm-thick Ag layer onto one side of the Pd layer to define the minimum conductive area of the upper electrode. The Ag layer maintains a consistent electrode size irrespective of H_2 presence, defining a stable base capacitance. Pd, due to its intrinsic properties, enables active H_2 dissociation on its surface and exhibits significant hydrogen solubility, with up to $PdH_{0.02}$ in the α phase and $PdH_{0.6}$ in the β phase,[42] along with rapid hydrogen diffusion rates.[43] In contrast, Ag has a high energy barrier for interaction with H_2, resulting in extremely low hydrogen solubility and diffusion rates,[44–50] without undergoing any phase transitions. We also observed no capacitance changes even at 4% H_2 exposure in an Ag/PDMS/Si sample without Pd (Figure S4, Supporting Information), confirming Ag's negligible interaction with H_2 and clean baseline stability. Consequently, capacitance changes are attributed dominantly to nanogap operations in the Pd regions. Upon exposure to an H_2 atmosphere, the Pd lattices absorb H atoms into their interstitial sites, causing lattice expansion.[51,52] When the nanogaps between the Pd islands are sufficiently narrow, this expansion closes the gaps at specific H_2 concentrations, thereby increasing the area of the upper electrode that is electrically connected to the Ag layer. This results in discrete increases in the capacitance signal (Figure 1b). At higher H_2 concentrations, the capacitance reaches saturation as the entire Pd area comes into contact with the Ag layer. Conversely, when the H_2 is removed, the Pd lattice contracts, causing the previously closed gaps to reopen, reducing the Pd area contact with the Ag electrode and bringing the capacitance signal back to its baseline level. It is crucial to note that the maximum and minimum capacitance values are determined by the areas of the sputtered Pd and Ag regions. Consequently, the sensor signal is confined within a specific range, enhancing its reliability compared to conventional resistive nanogap sensors.

Figure 1c demonstrates how capacitance in SANG sensors varies with changes in H_2 concentration. Because the nanogap network contains gaps of varying sizes, the wider gaps remain open, while the narrower gaps progressively close as the H_2 concentration increases. Therefore, the area of the connected Pd islands is dependent on the H_2 concentration, as verified by in situ OM images. A supplementary in situ OM video is provided to demonstrate the real-time operation of nanogaps under H_2 conditions in both the ON and OFF states, evidence of the reversible conversion between Pd and Pd hydride (see the Video S1, Supporting Information). Ultimately, the value of C is proportional to the area of the upper electrode, which comprises the union of the Ag layer area and the Pd islands in contact with the Ag layer $\left(A = A_{Ag} \cup \sum A_{Contacted\ Pd\ island}\right)$. We defined the sensor response as the normalized ratio of C change ($\Delta C/\Delta C_{max}$), where ΔC represents the change in capacitance ($C - C_0$) and ΔC_{max} is the difference between the maximum and baseline capacitance ($C_{max} - C_0$). The potential capacitance change in this sensor is primarily due to electrode area changes from nanogap behavior, with negligible contribution from PDMS-H_2 interaction (e.g., dielectric constant changes). H_2 exhibits very weak interactions with

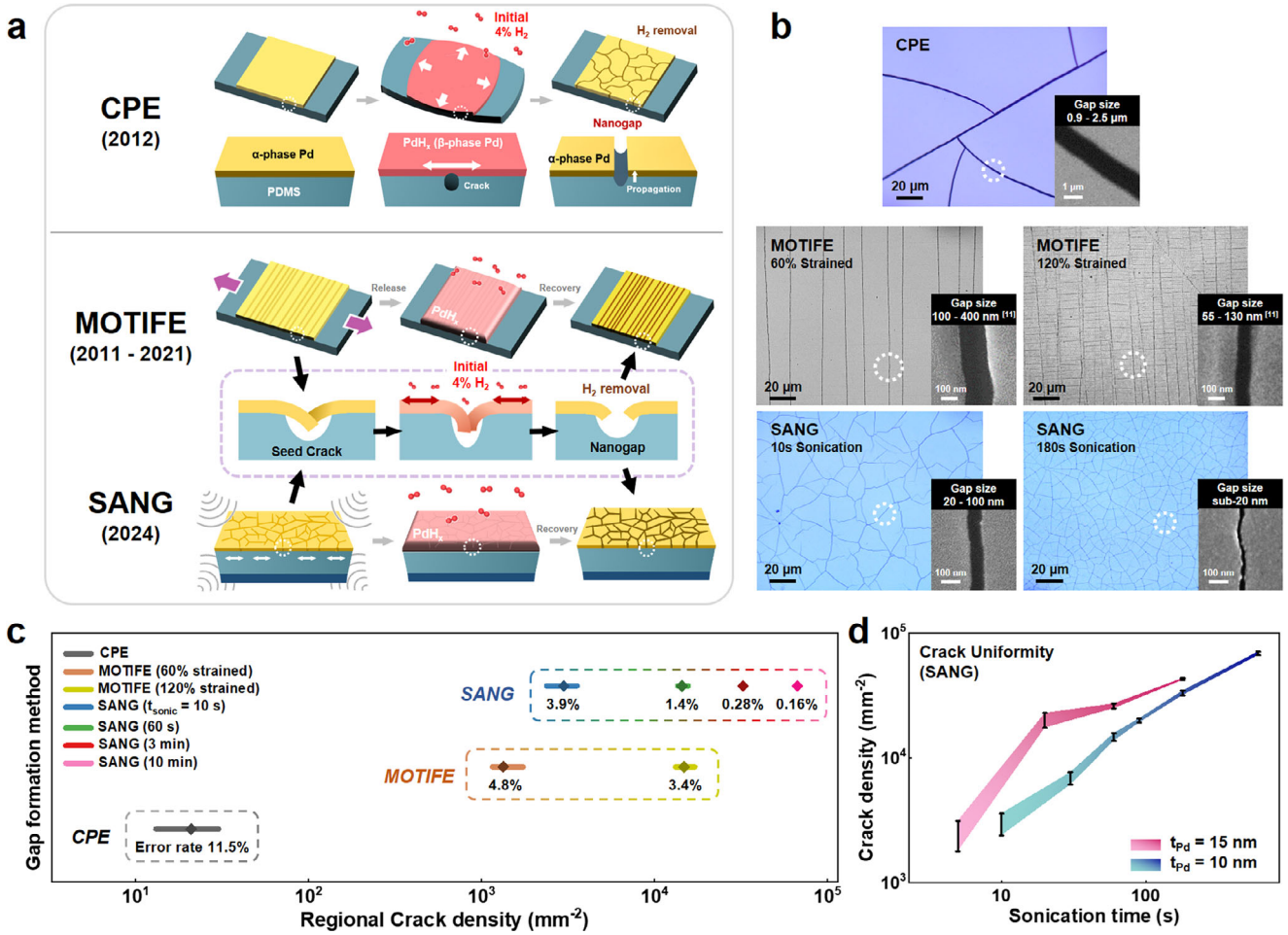

Figure 2. Comparison of various nanogap formation methods (CPE, MOTIFE, and SANG) that include the initial high-concentration H_2 exposure process. a) Schematic that outlines the formation and mechanism of nanogaps for each method. b) Comparison of OM and SEM images of nanogaps formed by each nanogap formation method. c) CPE, MOTIFEs (60% and 120% strained), and SANGs (t_{sonic} = 10 s, 60 s, 3 min, 10 min). The crack density was quantified by applying the same consistent calculation method to each type of nanogap, estimating the number of Pd fragments within a unit area (1 mm^2). The error rate of the regional crack density was calculated by analyzing OM images obtained from ten random spots on the Pd surface after nanogap formation. d) The distribution of regional crack density according to varying sonication time for two SANG samples with different Pd thicknesses (t_{Pd} = 10, 15 nm).

PDMS at room temperature and atmospheric pressure due to its low condensability and non-polar characteristics, showing even lower interaction levels than N_2.[53,54] Furthermore, the solubility of H_2 is reported to be the lowest among various gases,[53–56] being ≈10^{-5} times that of Pd.[40,42] This is also supported by the observations in the Ag/PDMS/Si sample (Figure S4, Supporting Information). The sensor unit was mounted on a micro-probe equipped with a mass flow controller (MFC) to monitor real-time capacitance changes between the two electrodes at room temperature (20 °C) using an LCR meter at a frequency of 1 kHz with an alternating voltage of 1 V. The dielectric loss was measured to be negligible under this setup. (See Note S2, Supporting Information).

Figure 2 compares the characteristics of SANG with previously established nanogap formation techniques, all of which involve inducing a phase transition in Pd by exposing it to an initial high concentration of H_2 (Figure 2a). In this study, we quantified the crack density—defined as the number of Pd fragments per unit area—allowing for a direct comparison of the different nanogap formation methods. Crack density was determined by counting the average number of intersections between the cracks and the horizontal and vertical grids observed in a 100× magnified OM image (Figure S5, Supporting Information). For CPEs,[17] cracks first form at the Pd/PDMS interface due to tensile stress from the areal expansion of Pd during the initial H_2 exposure. After dehydrogenation, as Pd reverts to the α-phase, these cracks penetrate through the Pd thin film, resulting in gaps as wide as 900 nm (Figure 2b). This large gap size is attributed to the absence of pre-existing seed cracks in Pd, which undergoes substantial deformation during the hydrogenation process. To validate this, we referenced a previous study on CPE to fabricate a 1 mm-thick unsupported PDMS substrate and performed nanogap formation experiments under identical conditions. The nanogap sizes we measured aligned with previously reported values. For highly mobile thin films on elastomers (MOTIFEs),[18–23] repeated cycles of mechanical stretching and release create parallel seed

cracks perpendicular to the strain direction in the Pd/PDMS system. These cracks evolve into operational nanogaps upon initial H_2 exposure through a mechanism similar to SANG. Since 2011, this stretching technique has been the most widely used for nanogap formation in Pd. Kim et al.[57] demonstrated that adjusting the strain (30%–120 %) during stretching could control the density of seed cracks, with higher crack density leading to smaller nanogap sizes and lower detection limits after initial H_2 exposure. We replicated these experiments using a micro-tensile tester under the same conditions for 60% and 120%-strained MOTIFE, achieving crack densities and nanogap sizes consistent with those reported in the literature.

For SANGs, extending the sonication time (t_{sonic}) for the Pd/PDMS/Si system resulted in an increased density of seed cracks and smaller gap sizes after the initial H_2 exposure. When t_{sonic} exceeded 3 min, SANGs exhibited extremely fine, uniformly distributed gaps across the Pd surface, which were notably smaller than those produced by the CPE and MOTIFE methods. Scanning electron microscopy (SEM) revealed that SANGs created with t_{sonic} longer than 3 min were narrower than 20 nm, which represents a significant reduction compared to previously reported nanogaps for H_2 sensors.[17–26] Accordingly, controlling the seed crack density is critical for fabricating tunable nanogap sensors, as higher crack densities result in more sensitive sensors with narrower gaps. This behavior can be explained as follows. During the initial H_2 exposure, the two Pd layers on either side of a crack underwent hydrogenation-induced deformation and corresponding substrate-constraint stress. This stress accumulated at the crack, causing it to expand into an electrically isolated nanogap once the H_2 was removed. Therefore, smaller Pd fragments that underwent limited deformation and stress during nanogap formation resulted in narrower gaps, which are essential for achieving low detection limits. The small gap sizes observed in SANGs and MOTIFEs with high crack densities were attributed to the limited deformation and minimized tensile stress accumulation experienced by the smaller Pd fragments during initial hydrogenation. Additional OM images of these nanogaps are provided in Figure S6 (Supporting Information). Figure 2c compares the average crack density and associated error across different areas for the three nanogap formation methods. The CPE method, with the lowest average crack density, exhibited the highest error across different regions, indicating an uneven distribution of nanogaps. In the MOTIFE method (with 60% and 120% strained, respectively), as the tensile strain increased, crack density increased while the error decreased. For SANG, when the sonication time exceeded 1 min, the crack density surpassed that of 120% strained MOTIFE, while exhibiting significantly lower error rates. Figure 2d shows the crack density curves for SANGs with different Pd thicknesses (t_{Pd} = 10, 15 nm) as a function of t_{sonic}. In both cases, error across different regions decreased with increasing t_{sonic}, leading to more uniform nanogaps. However, as t_{sonic} increased, the crack density of SANGs tended to converge along different trend lines depending on the dimension parameters of the Pd/PDMS system. This variation is attributed to the differing ability of the thin-metal film to accommodate deformation under mechanical stress, which depends on the thickness of the metal film on the soft substrate.[58] Additionally, the rate of increase in crack density with t_{sonic} gradually decreased, likely because the stress from sonication concentrated on existing cracks and was relieved by crack propagation, restricting the formation of new cracks. These results demonstrate that the sonication process is highly effective in applying uniform and omnidirectional stress to the Pd/PDMS system, resulting in consistent and dense crack morphologies. Given that MOTIFEs require a micro-tensile tester for precise strain control and a tensile speed of less than 1 mm s^{-1}, SANG sensors offer superior simplicity and process efficiency. This suggests that SANG could be a promising approach for the mass production of reliable nanogap sensors.

2.2. H_2 Sensing Performance for SANG Sensor

Figure 3 shows the H_2 sensing performance of our capacitive Pd nanogap sensor unit, which is configured with a Pd thin film/PDMS/doped Si structure. These capacitances increase and decrease curves are predominantly attributed to the repetitive contact and separation of the nanogaps driven by the expansion and contraction of the Pd lattice parameter, thereby providing experimental support for the reversible conversion between Pd and Pd hydride.

We experimentally demonstrated that the combination of sonication and subsequent 4% H_2 exposure cycles (200-s intervals) produced nanogaps capable of repeatable on/off operations (Figure 3a). It was observed that the baseline capacitance in the absence of H_2 gradually decreased with increasing cycles. This reduction was due to the development of sonication-induced seed cracks into stabilized nanoscale gaps, driven by plastic deformation in the Pd lattice and the accumulation of tensile stress during hydrogenation. These processes electrically isolated the Pd fragments. As H_2 exposure and removal were repeated, the number of electrically isolated Pd fragments eventually reached a saturation point, causing the area of the upper electrode before H_2 exposure to approximate the area of the Ag layer alone. After several cycles, the baseline capacitance stabilized and remained unchanged in subsequent cycles. The Ag layer deposited on one side of the Pd film maintained its structure regardless of H_2 presence, ensuring continuous contact and conductivity with the nearest Pd islands during and after hydrogenation. At this stage, the sensor unit produced signals with predefined maximum and minimum capacitance values, corresponding to the total area of the combined Pd and Ag layers and the area of the Ag layer alone, respectively. The consistent maintenance of the baseline capacitance after the formation of nanogaps serves as experimental evidence that the Ag layer retains a stable structure and area despite the repeated on/off cycling of H_2. This also experimentally confirms that the interaction between H_2 and Ag is minimal and does not affect the sensor's functionality. After the formation of the nanogaps, exposure to a low H_2 concentration of 400 ppm resulted in signal saturation in less than 10 s (Figure 3b). This rapid sensing response was attributed to the operation of sub-100 nm Pd gaps.[21,25,59] These results confirm the fineness and uniformity of SANGs, which exhibited consistent performance even at low H_2 concentrations, demonstrating the sensor's capability for rapid detection. However, at low concentrations where the response does not saturate to its maximum value, the reaction rate gradually decreases with decreasing concentration. Investigating the full response time at 10 ppm revealed a value of 830 s, which

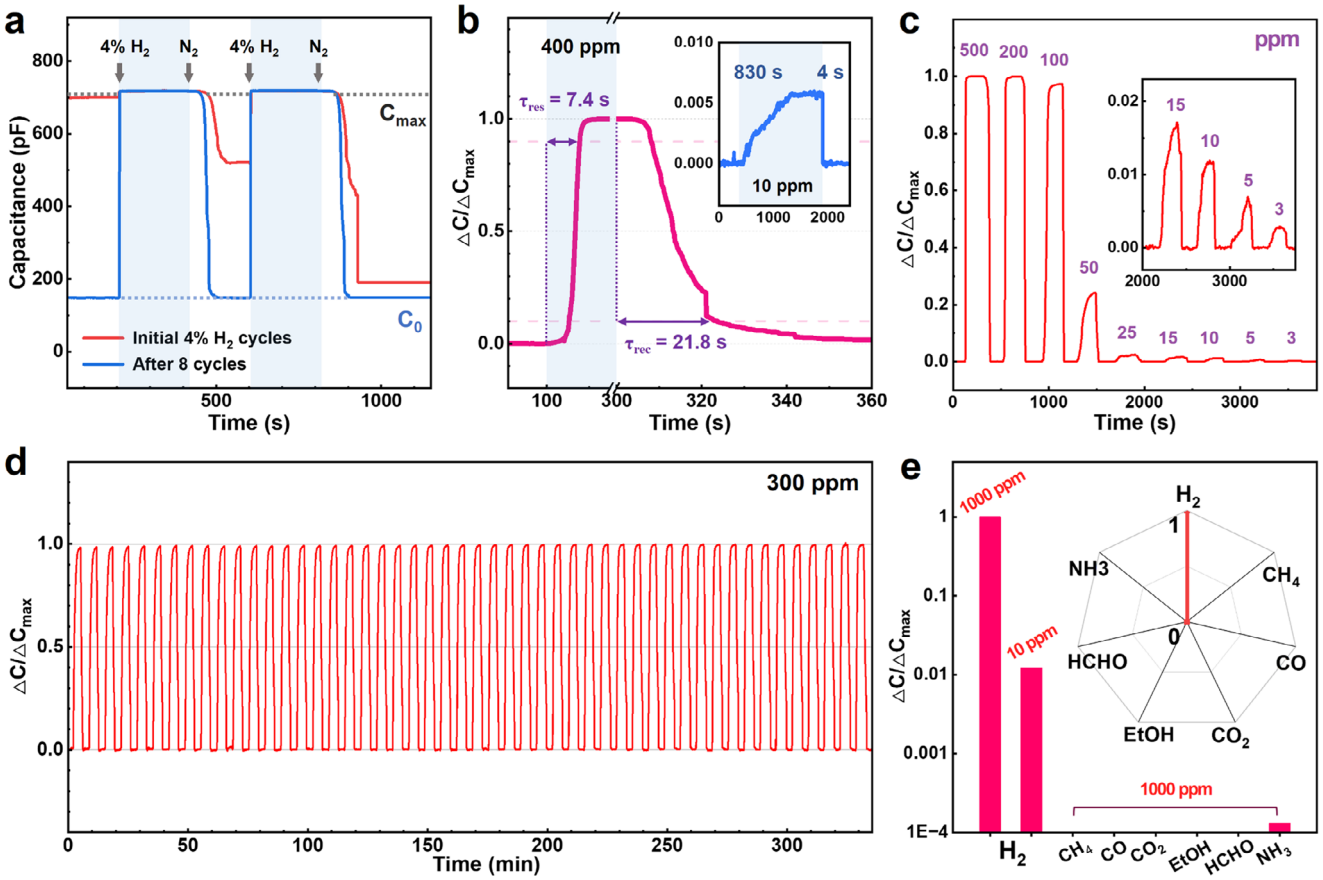

Figure 3. Characterization of nanogap formation and H_2 sensing test for SANG sensors. a) Capacitance response of the sensor before and after sonication, showing the effects of initial 4% H_2 exposure cycles. The maximum capacitance (C_{max}) is observed when the entire Pd and Ag layer functions as the upper electrode due to contact between the Pd gaps (gray line). After 20-s sonication, the seed cracks begin to develop into electrically operational nanogaps over the cycles (red curve). The capacitance signal reaches the base level (C_0), which does not decrease further with additional cycles (blue curve). b) Capacitance response to 400 ppm H_2 at room temperature with response time of 7.4 s and recovery time of 21.8 s. c) Sensitivity test over a range of H_2 concentrations (3–500 ppm), demonstrating the limit of detection (LOD) at 3 ppm with 200 s exposure and 200 s recovery intervals. d) Repeatability test showing the sensor response over 50 cycles of 300 ppm H_2 with 200 s exposure and 200 s recovery intervals. e) Selectivity test comparing the responses to 1000 and 10 ppm H_2 and other gases at 1000 ppm (CH_4, CO, CO_2, EtOH, and NH_3 in air balance, and HCHO in N_2 balance).

can be attributed to the kinetic interaction between the palladium lattice expansion and the hydrogenation rate. After signal saturation at 10 ppm, the recovery time was remarkably fast at ≈4 s. The response/recovery time was determined as the time required to reach 90% of the maximum signal intensity after H_2 reached the test chamber and was accurately calculated using a system in which the timing of the MFC control software and the LCR meter recording software was synchronized.

Figure 3c shows the real-time signal response of a sample fabricated via 5 min of sonication under various H_2 concentrations. At H_2 concentrations above 100 ppm, the signals saturated to a maximum value within 200 s, indicating that the entire film region became as conductive as the upper electrode, with most Pd gaps closed. At H_2 concentrations below 100 ppm, the responses diminished as the H_2 concentration decreased because some wide gaps remained open, reducing the effective area of the upper electrode and the resulting capacitances. Specifically, at concentrations below 50 ppm, the H_2 levels were insufficient to close most of the nanogaps in the Pd layer, meaning that only the few Pd islands nearest to the Ag region contributed to the signal. The LOD for our sensor was determined to be 3 ppm, the lowest LOD reported among Pd nanogap sensors to date.[59] This achievement is particularly noteworthy given that it was obtained at room temperature (20 °C), setting a significant benchmark even among other types of H_2 sensors operating under similar conditions.[60] This exceptionally low LOD of our sensor is based on its unique detection principle. In conventional resistive nanogap sensors, the LOD is determined by the minimum H_2 concentration required to establish a complete conductive path between the electrodes. Thus, the largest gap in the potential conduction path significantly impacts their sensing characteristics, even if narrow gaps exist within the Pd film. In contrast, our capacitive sensor generates a signal as long as one of the multiple Pd gaps closest to the Ag region closes, thereby connecting the Pd island to the upper electrode. This mechanism makes our sensors more reliable and sensitive to lower H_2 concentrations than resistive nanogap sensors, which are often difficult to predict in performance. Figure 3d shows the results of a

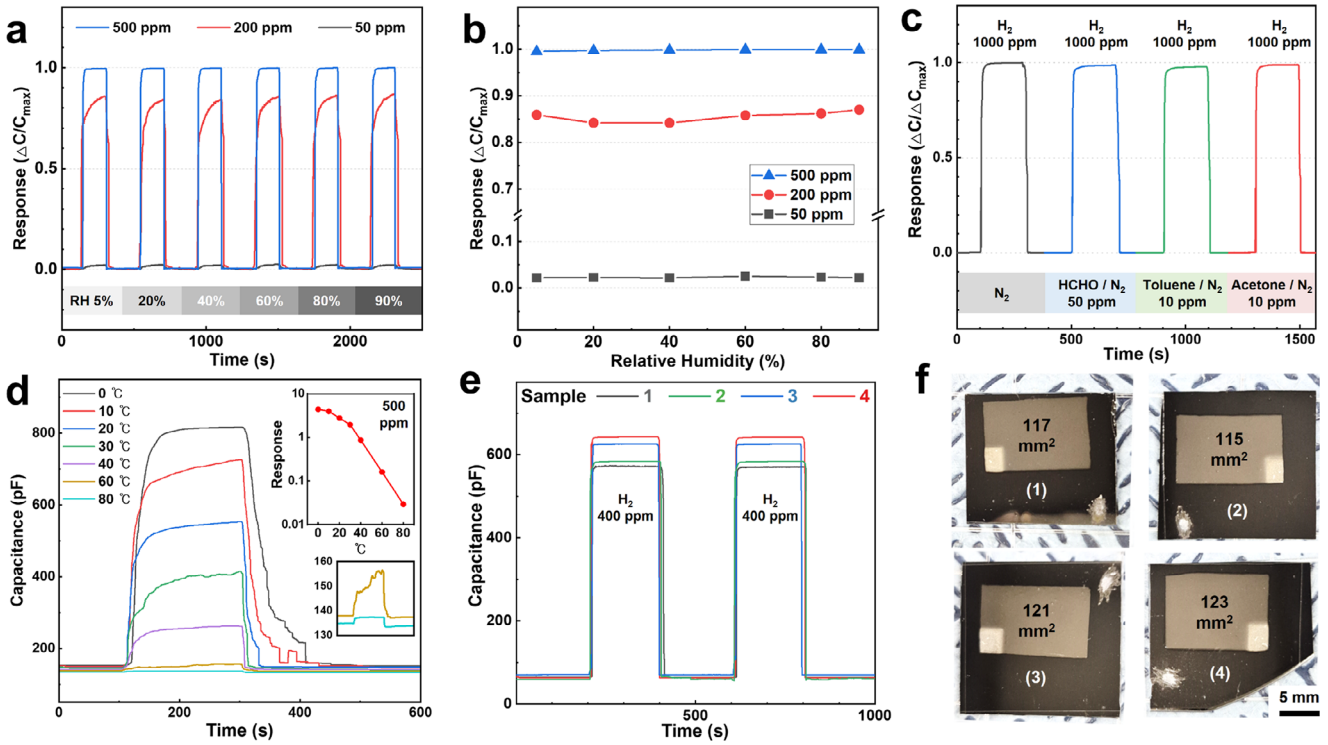

Figure 4. Humidity and temperature effects on the sensing performance and reproducibility test results. a) Capacitance response under varying humidity levels (RH 5%, 20%, 40%, 60%, 80%, 90%) for detecting H_2 concentrations (500, 200, 50 ppm) in N_2. b) Capacitance response as a function of relative humidity for detecting H_2 concentrations of 500, 200, and 50 ppm. c) Selectivity of the sensor for H_2 (1000 ppm) in the presence of interfering VOC gases (HCHO, toluene, acetone). d) Comparison of sensing properties (500 ppm H_2) at different temperatures (0, 10, 20, 30, 40, 60, 80 °C). e) Reproducibility of capacitance response across four sensor samples under 400 ppm H_2. The samples (1–4) were fabricated using 1-min sonication. f) OM images of the sensor samples (1–4).

perfect repeatability test conducted over 50 cycles at 300 ppm of H_2 – the lowest concentration tested in repeatability experiments for Pd nanogap sensors. For comparison, Pak et al. conducted a 50-cycle test with 0.5% H_2 using a Pd–Au nanoribbon array in 2019.[61] Our sensor's outstanding stability is attributed to the broad elastic region of PDMS, which effectively relaxed internal stress during Pd nanogap formation following sonication and initial 4% H_2 exposure.[15,33,34] Additionally, the extremely fine crack network created by the sonication process successfully limited the hydrogenation-induced strain on PDMS, minimizing PDMS cracking and resulting in stable elastic performance during cycling tests. The robust structural integrity provided by the rigid Si substrate support further enhanced the reliability of our sensor when utilizing Pd nanogaps for H_2 detection. We additionally included in Figure S7 (Supporting Information) the full real-time graph showing stable baseline and maximum capacitance over 94 cycles at 1000 ppm following an initial 4% H_2 cycle, as well as the 50-cycle repeatability test results at 10 ppm. Figure 3e shows the selectivity test for detecting 1000 ppm and 10 ppm H_2 in comparison with other test gases at the same 1000 ppm concentration. The results confirmed no response in detecting CH_4, CO, CO_2 EtOH, HCHO, and NH_3. This high selectivity is due to the fundamental operational principle of Pd nanogap sensors, which relies on the hydrogenation-induced mechanical expansion of the Pd lattice and consequent nanogap contact. The absorption and dissociation of H_2 by Pd, a metal renowned for its selective catalytic properties for H_2, occurred rapidly and selectively even at room temperature and atmospheric pressure. In contrast, other gases did not elicit a significant response with Pd, indicating the high H_2 selectivity and reliability of our sensors.[62] The full real-time capacitance graphs for each gas are provided in Figure S8 (Supporting Information).

2.3. Environmental Stability and Reproducibility

The stability under environmental factors such as temperature, humidity, and VOCs, and the reproducibility of the sensor were also evaluated (**Figure 4**). For the humidity tests, the total flow rate was maintained at 1000 sccm by adjusting the flow ratio between dry and humid gases at room temperature. We measured the sensor response at three H_2 concentrations (500, 200, 50 ppm) under varying humidity levels (RH 5%, 20%, 40%, 60%, 80%, 90%) (Figure 4a,b). We confirmed that humidity had no effect on the sensor's response or response time across a wide range of H_2 concentrations, demonstrating that the sensor reliably operates across a wide humidity range (RH 5%–90%). This aligns with previous studies on resistive nanogap H_2 sensors, which reported minimal influence of humidity.[23,62] Notably, the stable performance under H_2 concentrations below 200 ppm further highlights the high sensitivity and reliability of our sensor. We also monitored the real-time baseline capacitance while varying

the humidity levels (Figure S9, Supporting Information). The stable baseline capacitance, even under varying humidity, indicates no dimensional changes or swelling effects in the sensor. These results suggest that spin-coated PDMS on a Si wafer is an excellent choice as a dielectric for our capacitive H_2 sensor, providing sufficient flexibility for Pd nanogap operation while maintaining excellent structural stability and humidity resistance. PDMS is well-recognized for its superhydrophobic surface and outstanding water repellency, as demonstrated in various studies.[63–65] In addition, unlike chemiresistive sensors, the capacitive structure is largely unaffected by water molecules that may form on the metal surface under high-humidity conditions. This is supported by the absence of degradation trends in response characteristics during repeated exposure cycles conducted at RH 90%, although the response times were slightly slower than those observed at RH 0% (Figure S10, Supporting Information).

The VOC level experiment was conducted by measuring the maximum capacitance in the presence of 50 ppm HCHO, 10 ppm toluene, and acetone with 1000 ppm H_2 (Figure 4c). The results showed no significant changes in signal saturation, response time, or recovery time in the H_2 phase depending on the VOC level. The excellent H_2 selectivity of Pd nanogaps is consistent with the findings reported in previous studies.[62] This indicates that the VOC levels did not induce significant mechanical or dielectric coefficient changes in the PDMS. The sensor response at 500 ppm H_2 across a wide temperature range from 0 to 80 °C was examined (Figure 4d and inset). The response increased at lower temperatures, although it was slightly delayed. Conversely, at higher temperatures, the response decreased while the response rate improved. These results are consistent with the characteristics of resistive nanogap sensors previously reported.[23,66] At lower temperatures, the difference in the thermal expansion coefficients of PDMS and Pd causes PDMS to contract more than Pd, reducing the size of the Pd nanogaps. This leads to increased contact between the gaps at the same H_2 concentration, thereby enhancing the sensor response. Additionally, at lower temperatures, the hydride formation in Pd becomes more favorable, increasing hydrogen solubility.[40] This results in greater Pd expansion and more gap contacts at the same H_2 concentration. At higher temperatures, the nanogap size increases, and hydrogen solubility decreases, resulting in lower response. However, the diffusion of hydrogen within Pd is accelerated, improving the surface adsorption rate and thereby shortening the response time and the recovery time. There was no complete loss of the ability to detect low concentrations of 500 ppm, even at 80 °C, although the response decreased. Interestingly, the baseline capacitance exhibited about a 10% variation across the wide temperature range of 0–80 °C. This was attributed to the PDMS structure with minimal out-of-plane thermal expansion. The baseline signal of typical semiconductor-based chemiresistive sensors fluctuates with temperature, as their conductivity is governed by the exp(−kT) factor,[67] while optical sensors also exhibit signal drift due to temperature-induced changes in the refractive index. Given these limitations of other sensor types, this result underscores the reliability of our sensing mechanism across a wide temperature range.

To demonstrate reproducibility, we fabricated three additional samples under identical conditions (1-min sonication with the same Pd-Ag deposition ratio) and analyzed their baseline and maximum capacitance saturated at 400 ppm (Figure 4e,f). The four responses exhibited consistent trends, with an error rate of 5.7%. Considering that a hand-crafted mask was used during the sputtering process, these results demonstrate excellent reproducibility despite the simplicity of the fabrication process. This outcome is attributed to the capacitance variation range being geometrically predetermined by the deposition area of the electrodes. Unlike chemiresistive or optical sensors, which rely on the intrinsic electrochemical properties of materials and require complex material synthesis and fabrication processes, our sensors demonstrate superior reliability and a unique sensing mechanism. The sensitivity characteristics were also reproducible across samples with varying Pd dimensions (3×3, 5×5, and 10×10 mm^2) (Figure S11, Supporting Information). This reproducibility is attributed to consistent and uniform crack formation enabled by the sonication-assisted method, indicating the potential for practical applications through miniaturization to a packaging-compatible scale. These results demonstrate not only the performance reliability and reproducibility of our sensors but also the feasibility of wafer-scale fabrication (schematically illustrated in Figure S12, Supporting Information), supporting the potential for large-area production.

2.4. Tuning Sensing Characteristics via Sonication Time and PDMS Thickness

Figure 5 shows that by varying the initial t_{sonic}, the average nanogap size can be effectively controlled, allowing for the customization of the sensor's detection range. We fabricated three sensor units (A, B, and C) under identical conditions, using 10 nm-thick Pd layers on PDMS/Si substrates. The seed crack densities were adjusted by varying t_{sonic} to 10, 30, and 300 s, respectively. These sensors were then exposed to 4% H_2 cycles to form operational nanogaps, and their morphologies were compared using OM analysis (Figure 5a–c). SEM confirmed the size range of Pd nanogaps in each sample, revealing a gradual decrease in average nanogap size with increasing crack density, consistent with previous findings.[57] It was observed that longer sonication times resulted in a shift of the sensing range toward lower H_2 concentrations, accompanied by a corresponding decrease in both the LOD and signal saturation point (Figure 5d). This trend can be attributed to higher crack densities leading to smaller average nanogap sizes, which increases the probability of narrower nanogaps forming. Additionally, according to ref.[27], smaller Pd fragments experience less strain limitation from the substrate during the hydrogenation process. This suggests that the Pd lattice in smaller fragments can exhibit higher expansion rates at a given hydrogen concentration after nanogap formation. Consequently, longer sonication times not only reduce the gap sizes but also make them more prone to contact, increasing the likelihood of upper electrode area changes even at low hydrogen concentrations. This discussion provides an explanation for the experimental results of our sensor, where sensitivity improved with increasing sonication time. The calculated crack densities for samples A, B, and C, along with their real-time response curves for different H_2 concentrations, are shown in Figure S13 (Supporting Information). The concentration-dependent response characteristics of the sensor were further examined in Figure S14

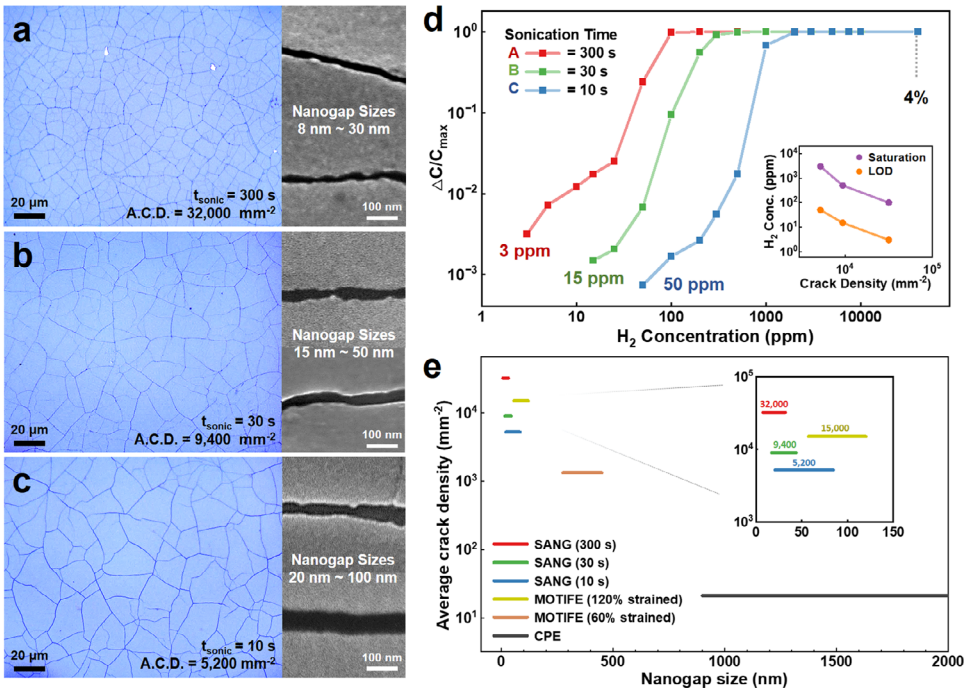

Figure 5. a–c) OM and SEM images of three SANG samples subjected to different initial t_{sonic}, illustrating the morphology and size distribution of nanogaps. The average crack density (A.C.D.) was also calculated. a) t_{sonic} = 5 min. b) t_{sonic} = 30 s. c) t_{sonic} = 10 s. d) Response curves to varying H_2 concentrations for the three types of SANG samples with different initial sonication times. The inset shows that higher crack densities in Pd nanogaps tended to decrease both the H_2 concentration at which the signal saturates and the LOD. e) 2D plot comparing the nanogap size distribution range and average crack density of CPE and MOTIFEs (60% and 120% strained) with the three types of SANG samples.

(Supporting Information) through detailed calibration curve modeling. Figure 5e shows a 2D plot comparing the crack density and gap size range of the three SANG sensors with different sonication times, referenced against the CPE and strain-controlled MOTIFE methods reproduced and investigated in the previous section. The results indicated that, regardless of the nanogap formation method, higher crack densities were consistently associated with smaller average nanogap sizes. In particular, for methods such as MOTIFE and SANG, where seed cracks evolve into nanogaps, it was observed that smaller Pd fragments led to less deformation and reduced tensile stress accumulation during the initial hydrogenation/dehydrogenation process, resulting in a reduction in average gap sizes.[21] For MOTIFEs, significant differences in crack density occurred in the horizontal and vertical directions relative to the stretching axis, leading to variations in nanogap sizes in each direction. However, for SANG, even just 30 s of sonication produced a crack density similar to that of 120%-strained MOTIFE, resulting in significantly narrower and more uniform nanogap sizes. This uniformity in gap size is attributed to the omnidirectional formation of Pd fragments due to sonication-induced stress, in contrast to the directional stretching in MOTIFE. These findings suggest that our SANG method offers a novel, simple, and tunable approach for uniform nanogap formation, enhancing the reliability and performance of Pd nanogap sensors.

We also discovered during the analysis of the effects of PDMS thickness that this parameter improves the linearity of the sensitivity curve and expands the linear dynamic concentration range (**Figure 6**). The PDMS layer thickness, like the Pd layer thickness, is a critical factor influencing the crack formation process and the mechanical behavior of the nanogaps. PDMS thickness directly determines the system's response to external stress, which in turn affects the seed crack density, the readability of nanogap formation, and the resulting nanogap size. By fabricating capacitive sensors with PDMS layers of different thicknesses while maintaining a consistent Pd thickness of 10 nm, we prepared three samples: 1) a sample with a PDMS thickness of 5 μm achieved by diluting PDMS in hexane at 1:6 ratios, 2) our standard sample with a 17 μm PDMS layer (diluting in 1:3 ratios), and 3) a sample with a bulk PDMS layer ≈400 μm thick (produced without spin-coating). Capacitive sensors were fabricated following the same procedure for all samples with 30-s sonication. Their OM images and sensor performance were compared. Figure 6a shows that the 5 μm PDMS sample exhibited significantly reduced seed crack density and poor crack morphology uniformity. We attribute this to the increased stiffness of the PDMS layer as it becomes thinner, similar to the behavior of the Si supporting substrate, which significantly reduces the mobility of the Pd thin film. This phenomenon can be explained by the shear-lag model in the Pd/PDMS heterostructure.[27] The thinner PDMS layer increases the stress required for crack initiation, hindering the uniform formation and propagation of cracks, and ultimately impeding the facile formation of nanoscale gaps. Capacitance measurements revealed that the number of initial high-concentration H_2 exposure cycles required to bring the sensor capacitance to the baseline level increased dramatically. While the standard sensor reached the baseline capacitance within 8 cycles of 4% H_2 exposure (Figure 6b), the 5 μm PDMS sample showed less than a

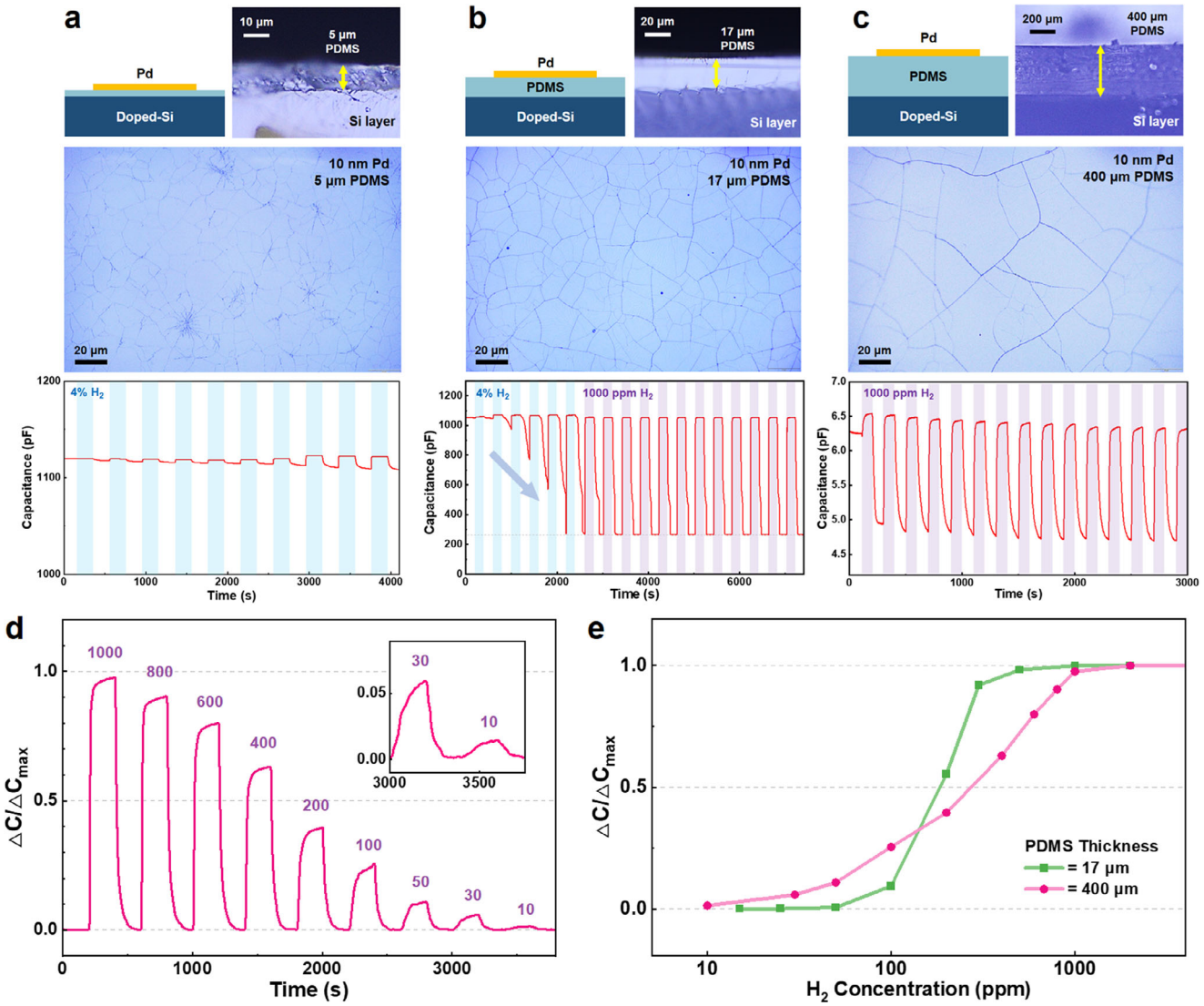

Figure 6. a–c) OM image of capacitance response of (a) a sample with a thinner PDMS layer (5 μm), b) a sample fabricated using the original process (17 μm PDMS), and c) a sample with a thicker PDMS layer (400 μm). Samples underwent an initial 30-s sonication during fabrication. d) Real-time capacitance response of the sensor unit with a 400 μm-thick PDMS layer under varying H_2 concentrations (1000–10 ppm). e) Sensitivity comparison between sensor units with different PDMS thicknesses: 17 μm (green line) and 400 μm (pink line). Both sensors were fabricated using 30 s of sonication.

1% reduction in capacitance even after 10 cycles. This indicates a significant degradation in the manufacturability of the sensor, one of its key advantages, and also leads to reduced sensitivity and reliability due to the non-uniform density and size of the nanoscale gaps. Conversely, the bulk PDMS sample with a thickness of 400 μm exhibited predictable crack morphology similar to that of the 17 μm sample (Figure 6c). The system capacitance decreased to below 10 pF, attributed to the increased electrode distance resulting from the thicker PDMS layer. This lower capacitance could potentially reduce signal resolution. Notably, seed cracks did not require a high H_2 concentration of over 1%–2%, typically necessary for PdH_x phase transition, to develop into operational nanogaps. Some of these cracks transformed into functional nanoscale gaps even under 1000 ppm H_2 cycles, forming a stable baseline. This behavior is attributed to the increased thickness of the PDMS layer, which minimizes the stiffness of the underlying substrate at the surface and enhances the mobility of the Pd film, thereby inducing significant deformation even with minimal hydrogenation. Additionally, increasing the sonication time (10, 30, 180, 300 s) resulted in higher crack density and progressively finer gap sizes (Figure S15, Supporting Information). As in previous sections, we calculated the areal crack density for each case, which was found to be lower than that of the original 17 μm samples. Interestingly, we found that using thicker PDMS allowed for more precise concentration differentiation and an extended sensing range, leading to an improvement in the linearity of the sensitivity curve with respect to concentration (Figure 6d,e). This effect is primarily attributed to the increased flexibility of the PDMS surface, which enhances the mobility of the Pd film and results in a more diverse distribution of gap sizes. Another reason for the improved linearity could be the shortened response time, attributed to the increased mobility

of the Pd film, which leads to a greater capacitance change over 200-s H_2 exposure.

In summary, the sensitivity of our sensor could be tuned by adjusting the sonication time, while the linear dynamic concentration range could be controlled by modifying the PDMS thickness. This tunability, achieved through such straightforward parameter adjustments, significantly enhances the versatility of our sensor, further increasing its potential for application across various industrial domains.

3. Conclusion

In this study, ultrasonication was used to create uniform seed cracks in 10 nm-thick Pd thin films on an elastomeric substrate, demonstrating its effectiveness in developing nanogap hydrogen sensors. By leveraging hydrogenation-driven phase transitions, we established ultrasonication as a reliable method for producing size-controllable Pd nanogaps. Unlike traditional resistive Pd nanogap sensors, our approach incorporated a stable Pd/PDMS/doped-Si system and a capacitive detection method, ensuring both sensitivity and structural stability. The sensor demonstrated exceptional sensitivity, repeatability, and selectivity at low H_2 concentrations, maintaining consistent performance over 50 cycles at 300 ppm H_2. The superhydrophobicity of PDMS and the capacitive mechanism ensured perfect humidity stability. Longer sonication times were found to produce smaller gaps, shifting sensitivity toward lower H_2 concentrations, while increasing the PDMS thickness tended to enhance the sensor's linear dynamic range. Notably, sub-20 nm gaps achieved with 5 min of sonication enabled a 3 ppm detection limit, marking a significant milestone for room-temperature H_2 sensors. Our integration of capacitive structures with Pd nanogaps not only enhances sensor stability but also boosts commercialization potential, contributing to the growth of the H_2-based economy. The tunability and ease of fabrication indicate strong potential for mass production, contingent on pre-investigation of characteristic curves. This advancement supports safe H_2 applications across various industries, enabling timely leak detection. Additionally, the sonication process can generally be applied to thin-metal-film/polymer heterosystems to facilitate uniform defect control, offering potential benefits for research in areas such as defect engineering for functional membranes,[68] crack-based lithography,[69] and crack-templated nanostructure fabrication.[70]

4. Experimental Section

Fabrication of Samples: A 4-inch B-doped Si wafer was used with a 2000 Å-thick SiO_2 layer as the substrate. A PDMS-based elastomer and curing agent (Sylgard 184, Dow Corning Corp.) were mixed in a 10:1 weight ratio. To this mixture, hexane (≥95%, Sigma–Aldrich) was added in a 3:1 weight ratio, followed by sonication for 30 min. The wafer was treated with O_2 plasma at 100 W for 3 min to enhance adhesion with the PDMS layer. The PDMS mixture was then spin-coated onto the wafer at 3000 rpm for 30 s, degassed at 60 °C for 10 min, and cured at 80 °C for 6 h, resulting in an ≈17 µm-thick PDMS layer. The wafer was subsequently cut into 1.8 × 1.8 cm^2 pieces, cleaned via sonication in acetone for 10 min, rinsed with IPA, and dried with N_2 gas. A Pd thin film was deposited onto the PDMS substrate using ultra-high-vacuum DC magnetron sputtering at a base pressure of 5 × 10^{-8} Torr. In an Ar atmosphere maintained below 2.4 × 10^{-3} Torr and a flow rate of 34 sccm, a 10 nm-thick Pd film was deposited on the PDMS/Si wafer substrates at a deposition rate of 3.5 Å s^{-1}, using a 99.9% pure Pd target at 20 W. ThePd thin film measuring 1 × 1 cm^2 was deposited at the center of a diced PDMS/Si wafer using PI tape as a mask.

Nanogap Formation: To form seed cracks in the Pd layer, which would later develop into nanosized gaps, the sample was ultrasonicated (POWERSONIC 405, HWASHIN) at maximum intensity in ethanol for durations ranging from 5 s to 5 min. Afterward, a 50 nm-thick Ag layer was sputtered onto one side of the cracked Pd layer to establish the minimum area of the upper electrode. To expand the sonication-induced Pd cracks into operational nanogaps, the sample was exposed to a high concentration of H_2 gas (4%, balanced with N_2) for 200 s in a chamber, followed by purging with N_2. These exposure cycles were repeated until the sample exhibited a stable base-level capacitance.

Characterization: Scanning electron microscopy (SEM, JSM-7800F, JEOL) and optical microscopy (OM, Olympus BX41M) were employed to examine the size of the Pd nanogaps and analyze the surface morphologies of the fabricated Pd/PDMS samples.

Sensor Characterization: The fabricated samples were configured to function as a capacitive H_2 sensor. The capacitance across the dielectric PDMS layer was measured using a Pd layer and a B-doped Si layer as the two electrodes, with an LCR meter (E4980A, Agilent) at a frequency of 1 kHz and an alternating voltage of 1 V. The performance of the capacitive H_2 sensor was evaluated using a microprobe station system (MPS-PT, Nextron) equipped with a mass flow controller (MFC). During the experiments, the temperature was precisely maintained at 20 °C using the microprobe station. The change in capacitance response over time was measured at various H_2 concentrations ranging from 1 ppm to 4%, with the H_2 concentration controlled by mixing H_2 gas (4%, 1%, 1000 ppm, and 10 ppm >99.999%) and N_2 gas (>99.999%) at 1 atm using the MFC.

Statistical Analysis: Quantitative analysis of crack density was performed using optical microscopy (OM) images acquired at 100× magnification, corresponding to a field of view of 0.030598 mm^2. For each sample condition, $n = 10$ randomly selected regions were analyzed. Crack density (mm^{-2}) was estimated using a grid-based method (Figure S6, Supporting Information), which showed less than 3% error compared to manual counts of Pd fragments. Outliers showing visible anomalies or atypical crack distributions were excluded, with at most two per group. Data were presented as mean ± standard deviation (SD). Statistical differences among groups were evaluated using one-way ANOVA, with significance defined as $p < 0.05$. All calculations and data visualizations were performed using OriginPro (OriginLab Corporation).

Supporting Information

Supporting Information is available from the Wiley Online Library or from the author.

Acknowledgements

S.L., J.L., and J.H. contributed equally to this work. This research was supported by the National Research Foundation of Korea (NRF) grant funded by the Korea government (MSIT) (No. NRF-2022M3H4A3053304, National Core Materials Research Center (Platform type)), Industry & Energy (MOTIE, Korea), a grant of Research and Development Program under the National Fire Agency (RS-2024-00404040) funded by Ministry of the Interior and Safety of Korea (MOIS, Korea), and the Deep Science Startup Promotion Program (RS-2025-02633929) supported by Commercializations Promotion Agency for R&D Outcomes (COMPA).

Conflict of Interest

The authors declare no conflict of interest.

Data Availability Statement

The data that support the findings of this study are available from the corresponding author upon reasonable request.

Keywords

capacitive, hydrogen sensor, Pd nanogaps, phase transition, sonication

Received: March 7, 2025
Revised: May 8, 2025
Published online:

[1] J. Jeon, S. J. Kim, *Energies* **2020**, *13*, 6263.
[2] T. Hübert, L. Boon-Brett, G. Black, U. Banach, *Sens. Actuators B: Chem.* **2011**, *157*, 329.
[3] M. A. Rosen, S. Koohi-Fayegh, *Energy Ecol. Environ.* **2016**, *1*, 10.
[4] Z. Wang, L. Zhu, J. Liu, J. Wang, W. Yan, *Energy Fuels* **2022**, *12*, 24614.
[5] Y. Jin, Z. Zheng, D. Wei, X. Jiang, H. Lu, L. Sun, F. Tao, D. Guo, Y. Liu, J. Gao, Y. Cui, *Joule* **2020**, *4*, 1714.
[6] F. A. A. Nugroho, I. Darmadi, L. Cusinato, A. Susarrey-Arce, H. Schreuders, L. J. Bannenberg, A. Bastos da Silva Fanta, S. Kadkhodazadeh, J. B. Wagner, T. J. Antosiewicz, A. Hellman, V. P. Zhdanov, B. Dam, C. Langhammer, *Nat. Mater.* **2019**, *18*, 489.
[7] H. M. Luong, M. T. Pham, T. Guin, R. P. Madhogaria, M.-H. Phan, G. K. Larsen, T. D. Nguyen, *Nat. Commun.* **2021**, *12*, 2414.
[8] W. Koo, H. Cho, D. Kim, Y. H. Kim, H. Shin, R. M. Penner, I. Kim, *ACS Nano* **2020**, *14*, 14284.
[9] M. T. Soo, K. Y. Cheong, A. F. M. Noor, *Sens. Actuators B: Chem.* **2010**, *151*, 39.
[10] Y. Hayashi, H. Yamazaki, K. Masunishi, D. Ono, T. Saito, N. Nakamura, A. Kojima, *Electr. Eng. Jpn.* **2021**, *214*, 23317.
[11] D. R. Baselt, B. Fruhberger, E. Klaassen, S. Cemalovic, L. C., S. V. Patel, T. E. Mlsna, D. McCorkle, B. Warmack, *Sens. Actuators B: Chem.* **2003**, *88*, 120.
[12] K. Christmann, *Surf. Sci. Rep.* **1988**, *9*, 1.
[13] C. Won, S. Lee, H. H. Jung, J. Woo, K. Yoon, J. Lee, C. Kwon, M. Lee, H. Han, Y. Mei, K.-I. Jang, T. Lee, *ACS Appl. Mater. Interfaces* **2020**, *12*, 45243.
[14] M. Cho, T. Kim, I. Cho, M. Gao, K. Kang, D. Yang, I. Park, *Langmuir* **2022**, *38*, 1072.
[15] F. Favier, E. C. Walter, M. P. Zach, T. Benter, R. M. Penner, *Science* **2001**, *293*, 2227.
[16] T. Kiefer, F. Favier, O. Vazquez-Mena, G. Villanueva, J. Brugger, *Nanotechnology* **2008**, *19*, 125502.
[17] J. Lee, J. Noh, S. Lee, B. Song, H. Jung, W. Kim, W. Lee, *Int. J. Hydrogen Energy* **2012**, *37*, 7934.
[18] T. Chang, H. Jung, B. Jang, J. Lee, J. Noh, W. Lee, *Sens. Actuators A* **2013**, *192*, 140.
[19] J. Lee, W. Shim, E. Lee, J. Noh, W. Lee, *Angew. Chem., Int. Ed.* **2011**, *50*, 5301.
[20] E. Lee, J. Lee, J. Noh, W. Kim, T. Lee, S. Maeng, W. Lee, *Int. J. Hydrogen Energy* **2012**, *37*, 14702.
[21] H. Jung, B. Jang, W. Kim, J. Noh, W. Lee, *Sens. Actuators B: Chem.* **2013**, *178*, 689.
[22] B. Jang, K. Y. Lee, J. Noh, W. Lee, *Sens. Actuators B: Chem.* **2014**, *193*, 530.
[23] S. Park, S. Lee, J. Jeong, D. Kim, H. Kim, H. Lee, W. Lee, *Sens. Actuators B: Chem.* **2021**, *348*, 130716.
[24] E. Menumerov, B. A. Marks, D. A. Dikin, F. X. Lee, R. D. Winslow, S. Guru, D. Sil, E. Borguet, P. Hutapea, R. A. Hughes, S. Neretina, *ACS Sens.* **2016**, *1*, 73.
[25] K. Hassan, T. Tung, P. Yap, M. Nine, H. Kim, D. Losic, *Anal. Chim. Acta* **2020**, *1138*, 49.
[26] J. Lee, M. Chung, K. Choi, J. Yoo, J. Yoon, presented at *2019 IEEE 32nd Int. Conf. on Micro Electro Mechanical Systems (MEMS)*, Seoul, Korea (South), January, **2019**.
[27] G. Kim, S. Lee, S.-k. Lee, H. J. Yu, H. Cho, Y. Chung, T.-E. Park, H.-S. Lee, W. Shim, K. H. Lee, J. Y. Park, Y. J. Kim, D. W. Chun, W. Lee, *Adv. Mater.* **2024**, *36*, 2310333.
[28] W. Lauterborn, W. Hentschel, *Ultrasonics* **1986**, *24*, 59.
[29] S. Howkins, *J. Acoust. Soc. Am.* **1966**, *39*, 55.
[30] C. Einhorn, J. Einhorn, J. L. Luche, *Synthesis* **1989**, *1989*, 787.
[31] M. Owen, P. Smith, *J. Adhes. Sci. Technol.* **1994**, *8*, 1063.
[32] D. Fuard, T. Tzvetkova-Chevolleau, S. Decossas, P. Tracqui, P. Schiavone, *Microelectron. Eng.* **2008**, *85*, 1289.
[33] P. Yoo, H. Lee, *Macromolecules* **2005**, *38*, 2820.
[34] D. Khang, J. Rogers, H. Lee, *Adv. Funct. Mater.* **2008**, *18*, 1.
[35] C. Chen, S. Yang, *Polym. Int.* **2012**, *61*, 1041.
[36] J. E. Worsham Jr., M. K. Wilkinson, C. G. Shull, *J. Phys. Chem. Solids* **1957**, *3*, 303.
[37] S. Wagner, T. Kramer, H. Uchida, P. Dobron, J. Cizek, A. Pundt, *Acta Mater.* **2016**, *109*, 114.
[38] N. Verma, R. Delhez, N. Van Der Pers, F. Tichelaar, A. Böttger, *Int. J. Hydrogen Energy* **2021**, *46*, 4137.
[39] A. Maeland, T. B. Flanagan, *J. Phys. Chem.* **1964**, *68*, 1419.
[40] R. Lässer, K. Klatt, *Phys. Rev. B* **1983**, *28*, 748.
[41] A. K. M. F. Kibria, Y. Sakamoto, *Mater. Sci. Eng. B* **1998**, *53*, 256.
[42] A. Maeland, T. B. Flanagan, *Platinum Met. Rev.* **1966**, *10*, 20.
[43] D. M. Nace, J. G. Aston, *J. Am. Chem. Soc.* **1957**, *79*, 3627.
[44] H. Katsuta, R. B. McLellan, *Scr. Metall.* **1979**, *13*, 65.
[45] H. Kimizuka, M. Shiga, *Phys. Rev. Mater.* **2021**, *5*, 065406.
[46] D. N. Jewett, A. C. Makrides, *Trans. Faraday Soc.* **1965**, *61*, 932.
[47] P. R. Subramanian, *J. Phase Equilibria* **1991**, *12*, 649.
[48] E. W. R. Steacie, F. M. G. Johnson, *Proc. R. Soc. A* **1928**, *117*, 778.
[49] Y. Li, Y.-T. Cheng, *Int. J. Hydrogen Energy* **1996**, *21*, 281.
[50] V. N. Verbetsky, S. V. Mitrokhin, *Solid State Phenom.* **2000**, *73-75*, 503.
[51] R. Chattot, I. Martens, M. Mirolo, M. Ronovsky, F. Russello, H. Isern, G. Braesch, E. Hornberger, P. Strasser, E. Sibert, M. Chatenet, V. Honkimäki, J. Drnec, *J. Am. Chem. Soc.* **2021**, *143*, 17068.
[52] C. Berlinguette, Y. Chiang, J. Munday, T. Schenkel, D. Fork, R. Koningstein, M. Trevithick, *Nature* **2019**, *570*, 45.
[53] Z. P. Smith, R. R. Tiwari, T. M. Murphy, D. F. Sanders, K. L. Gleason, D. R. Paul, B. D. Freeman, *Polymer* **2013**, *54*, 3026.
[54] T. C. Merkel, V. I. Bondar, K. Nagai, B. D. Freeman, I. Pinnau, *J. Polym. Sci., Part B: Polym. Phys.* **2000**, *38*, 415.
[55] I. Pinnau, Z. He, *J. Membr. Sci.* **2004**, *244*, 227.
[56] Y. Kamiya, Y. Naito, K. Mizoguchi, K. Terada, J. Moreau, *J. Polym. Sci. Part B: Polym. Phys.* **1997**, *35*, 1049.
[57] S. Kim, H. Lee, B. Jang, S. Cho, W. Lee, *J. Mater. Sci.* **2016**, *51*, 4530.
[58] T. Li, Z. Huang, Z. Suo, S. Lacour, S. Wagner, *Appl. Phys. Lett.* **2004**, *85*, 3435.
[59] H. Lee, J. Kim, H. Moon, W. Lee, *Adv. Mater.* **2021**, *33*, 2005929.
[60] S. Li, S. Zhou, S. Zhao, T. Jin, M. Zhong, Z. Cen, P. Gao, W. Yan, M. Ling, *Chemosensors* **2023**, *11*, 344.
[61] Y. Pak, Y. Jeong, N. Alaal, *Adv. Mater. Interfaces* **2019**, *6*, 1801442.
[62] W. Kim, B. Jang, H. Lee, W. Lee, *Sens. Actuators B: Chem.* **2016**, *224*, 547.
[63] F. Wang, S. Lei, J. Ou, W. Li, *Appl. Surf. Sci.* **2020**, *507*, 145016.
[64] H. Liu, J. Y. Huang, Z. Chen, G. Q. Chen, K. Q. Zhang, S. S. Al-Deyab, Y. K. Lai, *Chem. Eng. J.* **2017**, *330*, 26.
[65] C. Y. Cao, M. Z. Ge, J. Y. Huang, S. Li, S. Deng, S. Zhang, Z. Chen, K. Zhang, S. S. Al-Deyab, Y. Lai, *J. Mater. Chem. A* **2016**, *4*, 12179.
[66] B. Jang, W. Kim, M. Song, W. Lee, *Sens. Actuators B* **2017**, *240*, 186.
[67] A. Dey, *Mater. Sci. Eng. B* **2018**, *229*, 206.
[68] S. Li, W. Han, Q. An, K. Yong, M. Yin, *Adv. Funct. Mater.* **2023**, *33*, 2303447.
[69] S. Walia, R. Gupta, K. D. M. Rao, G. U. Kulkarni, *ACS Appl. Mater. Interfaces* **2016**, *8*, 23419.
[70] R. Adelung, O. C. Aktas, J. Franc, A. Biswas, R. Kunz, M. Elbahri, J. Kanzow, U. Schürmann, F. Faupel, *Nat. Mater.* **2004**, *3*, 375.